

Red quasars blow out molecular gas from galaxies during the peak of cosmic star formation

H. R. Stacey,^{1*} T. Costa,¹ J. P. McKean,^{2,3} C. E. Sharon,⁴ G. Calistro Rivera,⁵
E. Glikman⁶ and P. P. van der Werf⁷

¹Max Planck Institute for Astrophysics, Karl-Schwarzschild Str. 1, D-85748 Garching bei München, Germany

²ASTRON, Netherlands Institute for Radio Astronomy, Oude Hoogeveensedijk 4, 7991 PD, Dwingeloo, The Netherlands

³Kapteyn Astronomical Institute, University of Groningen, PO Box 800, 9700 AV Groningen, The Netherlands

⁴Yale-NUS College, Singapore, 138527, Singapore

⁵European Southern Observatory (ESO), Garching bei München, Germany

⁶Department of Physics, Middlebury College, Middlebury, VT 05753, USA

⁷Leiden Observatory, Leiden University, PO Box 9513, NL-2300 RA Leiden, The Netherlands

Accepted 2022 September 23. Received 2022 August 31; in original form 2022 July 18

ABSTRACT

Recent studies have suggested that red quasars are a phase in quasar evolution when feedback from black hole accretion evacuates obscuring gas from the nucleus of the host galaxy. Here, we report a direct link between dust-reddening and molecular outflows in quasars at $z \sim 2.5$. By examining the dynamics of warm molecular gas in the inner region of galaxies, we find evidence for outflows with velocities 500–1000 km s⁻¹ and timescales of ≈ 0.1 Myr that are due to ongoing quasar energy output. We infer outflows only in systems where quasar radiation pressure on dust in the vicinity of the black hole is sufficiently large to expel their obscuring gas column densities. This result is in agreement with theoretical models that predict radiative feedback regulates gas in the nuclear regions of galaxies and is a major driving mechanism of galactic-scale outflows of cold gas. Our findings suggest that radiative quasar feedback ejects star-forming gas from within nascent stellar bulges at velocities comparable to those seen on larger scales, and that molecules survive in outflows even from the most luminous quasars.

Key words: quasars: general – galaxies: high-redshift – galaxies: evolution – ISM: jets and outflows – submillimetre: ISM

1 INTRODUCTION

State-of-the-art cosmological simulations and semi-analytic models of galaxy evolution invoke strong feedback from active galactic nuclei (AGN) in order to explain the observed properties of massive galaxies across cosmic time (Di Matteo et al. 2005; Somerville & Davé 2015; Schaye et al. 2015; Weinberger et al. 2017; Dubois et al. 2021). The injection of energy and momentum into the galactic interstellar medium (ISM) and circumgalactic medium by quasar winds and/or radio jets are predicted to regulate star formation in massive galaxies (Fabian 2012). This feedback is also thought to produce the observed scaling relations (King 2005; Costa et al. 2014) between galaxy properties (e.g. Ferrarese & Merritt 2000) which already established by cosmic noon ($z \sim 2 - 3$; Förster Schreiber & Wuyts 2020). However, the physical channels allowing energy and momentum released on sub-pc-scales to affect gas on galactic scales remain largely unconstrained from both theoretical and observational perspectives (Harrison 2017; Harrison et al. 2018, for review). In particular, the question of whether AGN feedback operates predominantly via bulk ejection of the ISM or via prevention of cooling in the halo remains open. The answer to this question has profound implications on the nature of galaxy quenching and the ability of supermassive black holes to regulate their growth.

The most energetic class of AGN are quasars. Type 1 quasars are characterised by broad ionic or Balmer emission lines (FWHM > 1000 km s⁻¹). The majority of known quasars have unobscured optical continuum emission, although a subset (20–30 percent; Glikman et al. 2018b) have been identified with reddened optical/infrared spectra. The nature of these reddened quasars has been a topic of debate for at least 20 years (Webster et al. 1995). One might assume that they could fit into a scheme of AGN unification (Antonucci 1993; Urry & Padovani 1995) where the apparent quasar reddening is simply an effect of viewing angle, and broad line emission is observed but partially obscured by dust in the surrounding torus. However, many studies have found distinct properties of reddened quasars, indicating that they are intrinsically different from their bluer counterparts. Reddened quasars have significantly enhanced compact radio emission (Klindt et al. 2019; Rosario et al. 2020; Fawcett et al. 2020), which may be linked to shocks from winds rather than the nucleus (Hwang et al. 2018; Rosario et al. 2021). Reddened quasars are also linked with higher-velocity outflows of ionised gas (Urrutia et al. 2009; Perrotta et al. 2019; Temple et al. 2019; Vayner et al. 2021; Calistro Rivera et al. 2021; Monadi & Bird 2022), may have a different luminosity function (Banerji et al. 2015) and may have a higher incidence of mergers (Glikman et al. 2015; Zakamska et al. 2019). Furthermore, Calistro Rivera et al. (2021) found no difference in torus column density in a large systematic study of the broad-band spectral energy distributions (SED) of red and blue quasars in SDSS.

* E-mail: stacey@mpa-garching.mpg.de

Altogether, this evidence strongly disfavours orientation as the primary explanation for reddening. The rarity of reddened quasars and the high incidence of outflows has led many studies to propose that they are caught in a short-lived ‘blow-out’ phase in their evolution where rapid black hole accretion creates strong AGN feedback but has not yet cleared the nucleus of gas and dust (e.g. Glikman et al. 2012; Banerji et al. 2015; Calistro Rivera et al. 2021; Vayner et al. 2021).

An abundance of dust is conducive to strong quasar feedback. By enhancing the absorption cross section to UV and optical AGN radiation, the dusty ISM can, in principle, be driven out by radiation pressure, thereby reducing the supply of gas for star formation in the inner region of the galaxy (Fabian et al. 2008, 2009; Raimundo et al. 2010; Ishibashi et al. 2018) and resulting in correlations between galaxy bulge properties and black hole mass in agreement with observations (Fabian 1999). Radiation pressure on dust is predicted to operate and launch outflows at galactic scales on 100pc – 1kpc scales directly, as demonstrated by recent radiation-hydrodynamic simulations (Bieri et al. 2017; Costa et al. 2018a,b). It may also launch fast winds from galactic torus scales (\sim pc) (Roth et al. 2012), which shock-heat and generate hot, over-pressurised bubbles at larger scales (Costa et al. 2020). Alternatively, ultra-fast winds with speeds $\sim 0.1c$ can be driven out directly from accretion discs, though not via coupling to dust (which is expected to sublimate at those scales) but via radiation pressure on UV lines (e.g. Nomura & Ohsuga 2017) or magnetically (e.g. Fukumura et al. 2018).

From an observational perspective, unobscured Type 1 quasars are ubiquitously associated with outflows of ionised gas (e.g. Liu et al. 2013; Rupke et al. 2017). However, the fuel for star formation is in the molecular phase, so observations of outflows of molecular gas can directly trace the impact of AGN feedback on the star formation. With the advent of the Atacama Large (sub-)Millimetre Array (ALMA), much attention has been paid to the search for molecular outflows from quasar host galaxies at high redshift. Most studies have focused on low-excitation CO emission or [CII], which probe the extent of the gas reservoir (e.g. Sharon et al. 2016; Neeleman et al. 2021), but evidence for widespread molecular outflows at high redshift ($z > 1$) or higher AGN luminosities ($> 10^{46}$ ergs s^{-1}) is lacking. Some have found evidence for massive outflows of cold gas from quasar hosts on scales 10s–100s kpc (Bischetti et al. 2019; Cicone et al. 2021), although this does not appear to be ubiquitous (Novak et al. 2020) and may be difficult to disentangle from bulk gas in the galaxy, mergers/companions and star-formation-driven outflows. It has been suggested that molecular gas is destroyed in the most energetic systems such that only ionised outflows are observed (Fiore et al. 2017).

To test this hypothesis, we have studied a sample of sixteen Type 1 quasar hosts at $z > 1$ with carbon-monoxide (CO) molecular line measurements at rotational level transition $J_{\text{up}} \geq 7$. These lines probe warm, dense gas in the inner part of the galaxy ($\lesssim 1$ kpc; Stacey et al. 2021) that may be heated by the AGN radiation field (Weiß et al. 2007; van der Werf et al. 2010; Carniani et al. 2019). Here, we find distinct properties of high- J CO lines for red quasars that we attribute to outflow dynamics. In Section 2 we present the sample selection and introduce our new observations. In Section 3, we explain the SED modelling and lens modelling of the lensed quasar systems. In Section 4 discuss the evidence for molecular outflows and the possible scenarios that might explain the differences in CO properties. In Section 5, we discuss the quasar feedback mechanisms that could power the molecular outflows. In Section 6, we consider the implications for our results for galaxy and quasar evolution, and discuss avenues for future work. Throughout, we assume

the Planck Collaboration et al. (2016) flat Λ CDM cosmology with $H_0 = 67.8$ km s^{-1} Mpc $^{-1}$, $\Omega_M = 0.31$ and $\Omega_\Lambda = 0.69$.

2 OBSERVATIONS

For our analysis, we searched the literature and the ALMA archive for observations of Type 1 quasars in $J \geq 7$ CO lines. All these observations have sub-arcsecond angular resolution to account for any companions that may contaminate our measurements. Most of these quasars are strongly-lensed and were discovered in optical/infrared surveys.

2.1 ALMA observations

In addition to CO, [CI] and [CII] measurements obtained from the literature, we present new ALMA data for several objects. These observations are summarised in Table 1. Where we observe the CO (7–6) lines we also observe the [CI] (2–1) line simultaneously. Each data set was calibrated and reduced using the ALMA pipeline in CASA (McMullin et al. 2007). The calibrated data were inspected to confirm the quality of the pipeline calibration. We self-calibrated the data for SDSS J1330+1810 using the continuum-only spectral windows with a single solution interval for each antenna in both amplitude and phase. For MG J0414+0534, we performed phase calibration with a solution interval of 240 seconds.

We created a clean image cube of the spectral window containing the line emission with natural weighting of the visibilities (images are shown in Fig. A1 of the Appendix) and extracted a spectrum in an aperture around the lens. The line profiles (presented here and in the literature) do not show asymmetries that would indicate that their shapes are strongly affected by differential magnification (Fig. 1). J1042+1641 is a possible exception, although this may be explained by the signal-to-noise ratio of the data.

To measure the line width, we fit the line profiles with a single Gaussian, taking into account the noise in each channel. For MG J0414+0534, the CO (7–6) line is so broad that it is blended with the [CI] (2–1) line. We fit Gaussians to both lines simultaneously with the systemic redshift fixed to the value found for the molecular gas (Barvainis et al. 1998; Stacey et al. 2020). For SDSS J1330+1810, part of the [CI] line falls outside the spectral window. For these two cases, the integrated line luminosity is estimated from the fitted Gaussian profile rather than directly from the image. The line profiles and Gaussian fits for these ALMA observations are shown in Fig. 1.

2.2 NOEMA observations

We present new data from the WideX correlator on the Northern Extended Millimetre Array (NOEMA) of CO (3–2) line emission from MG J0414+0534. Data calibration, flagging for data quality, and imaging were carried out using the IRAM GILDAS package (Guilloteau & Lucas 2000). The standard calibration pipeline was lightly modified to compensate for poor weather, low elevation observations, and source brightness. The modifications include relaxing data flagging conditions (with some manual flagging as necessary), applying a separate phase correction based on water vapour radiometer observations over a longer scan period, and self-calibration using the line-free channels of MG J0414+0534. Due to the high signal-to-noise ratio of the observations, self-calibration required two model regions: an elliptical Gaussian and a point source, corresponding to the South-East image pair and Northern image, respectively, as

Table 1. New ALMA and NOEMA observations presented in this work. We give the project code, the synthesised beam FWHM (Θ_{beam}) used to extract the line profile and continuum flux density, the continuum frequency (ν_{cont}), the continuum flux density (S_{ν}) and the integrated line intensity (I_{line}) based on a Gaussian fit to the line profile(s). † denotes cases where we have applied a uv taper to the data weights to improve surface brightness sensitivity. *For these cases, the line intensity is approximated from the Gaussian fit to the line profile (see Section 2).

Project	Name	Line(s)	Θ_{beam} (arcsec)	ν_{cont} (GHz)	S_{ν} (mJy)	I_{line} (Jy km s ⁻¹)
S17BV	MG J0414+0534	CO (3–2)	7.8×2.7	96	34.8 ± 0.5	$3.1 \pm 0.4^*$
2018.1.01008.S	MG J0414+0534	CO (7–6); [CI] (2–1)	$0.3 \times 0.3^\dagger$	236	10.1 ± 0.4	7.8^* ; 3.7^*
2019.1.00948.S	SDSS J1330+1810	CO (7–6); [CI] (2–1)	0.5×0.4	342	6.3 ± 0.2	3.5 ± 0.2 ; 3.9^*
2019.1.00964.S	DES J0408–5354	CO (7–6); [CI] (2–1)	$1.2 \times 1.1^\dagger$	247	3.0 ± 0.4	4.9 ± 0.7 ; 3.3 ± 0.5
	J1042+1641	CO (10–9)	0.9×0.7	256	2.0 ± 0.3	4.0 ± 0.7

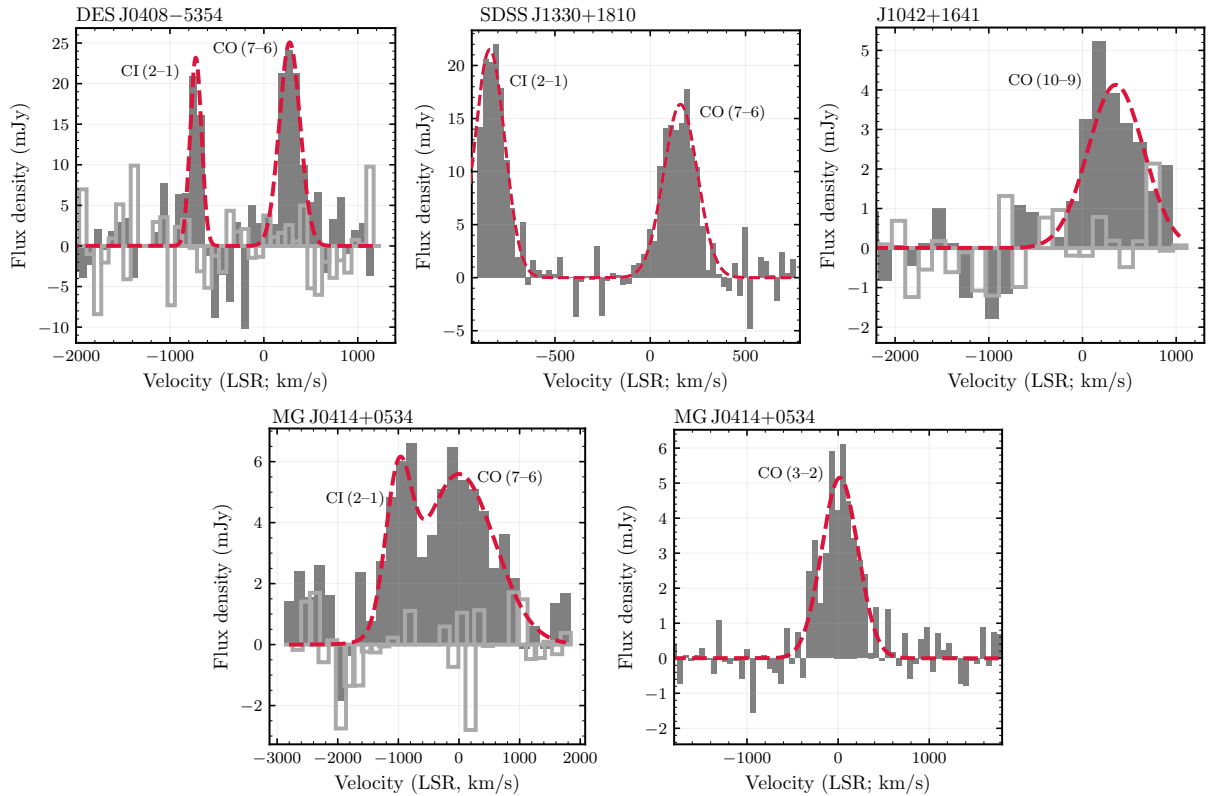


Figure 1. Line profiles for the new ALMA and NOEMA data presented in this work. The spatially-integrated line profiles (solid grey) and Gaussian fits to the CO and [CI] (2–1) line emission (red). Noise in the adjacent spectral window is shown in light grey unfilled bars for the noisier spectra. For all except MG J0414+0534 (bottom row), the systemic redshift is based on optical spectroscopy so a velocity offset in the CO is most likely because the ionic/Balmer lines trace out-flowing gas.

seen in prior higher angular resolution images of this gravitationally lensed system.

To create a continuum-free image cube, we performed continuum subtraction in Fourier space using standard GILDAS routines. Due to substantial side lobes in the synthesised (dirty) beam caused by the low-elevation/short-duration observations, we used a custom beam fitting script to determine the size of the central peak for the clean beam. The spatially integrated line profile was extracted in the same method as for the ALMA observations and the line width and integrated line flux was measured by fitting a single Gaussian.

3 MODEL FITTING

3.1 Lens modelling

Reconstruction of lensed emission may be performed assuming parametric sources (Spilker et al. 2016) or pixellated sources (Stacey et al. 2021), depending on the science goal and data quality. We choose a parametric source as we are interested in extracting a measure of the intrinsic source size and the data quality is generally not sufficient to allow for more freedom in the source surface brightness distribution.

We perform lens modelling for ALMA data using the software VISILENS (Spilker et al. 2016) that fits the visibility data directly to avoid errors introduced by deconvolution and sparse coverage of the Fourier plane. The model parameters are inferred using a Markov

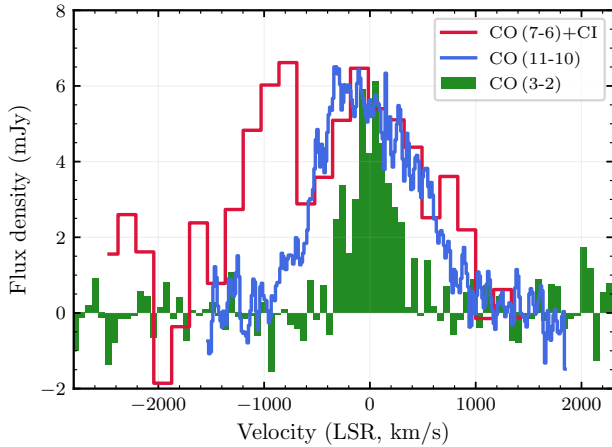


Figure 2. Comparison of CO line profiles for MG J0414+0534. While the CO (7–6) and [CI] (2–1) lines are blended, the CO (7–6) is similar to the CO (11–10) while both are clearly broader than the CO (3–2). This suggests that the CO (7–6) and CO (11–10) both probe different dynamics than the CO (3–2). The systemic redshifts of these lines are all consistent.

chain Monte Carlo method. We adopt fiducial lens models from the literature consisting of a singular isothermal ellipsoid and external shear, and in some cases an additional singular isothermal sphere for a companion galaxy. We model the source as a Gaussian or several Gaussians. The details of the fits to the continuum and integrated line emission are given in Table B1 of the Appendix. Images of the maximum a-posteriori lens models are shown in Figs. A2–A11 of the Appendix.

For MG J0414+0534, approximately half of the continuum emission at 350 GHz is due to synchrotron emission from the AGN (Stacey & McKean 2018). This complicates the lens modelling as the compact emission is thought to be affected by dark matter structure (Stacey & McKean 2018). We attempt to overcome this by making a deconvolved image with superuniform weighting (0.1 arcsec resolution) where the compact, high-brightness-temperature emission dominates the signal. We subtracted these CLEAN components from the visibility data such that the remaining emission is assumed to be only the dust continuum. This is not a perfect decomposition of the source emission mechanisms, but sufficient to estimate the magnification of the dust.

3.2 AGN luminosity, extinction and black hole masses

We use AGNFITTER (Calistro Rivera et al. 2016) to fit the broadband SED of each quasar and host galaxy. This software includes accretion disc, torus, host galaxy and starburst templates (Calistro Rivera et al. 2016, 2021). The accretion disc component is reddened by an SMC extinction dust law (Prevot et al. 1984) parameterised by rest-frame E_{B-V} . We compile photometry from all-sky surveys, where available, or from the literature.

We assume a minimum uncertainty of 10 percent on photometric measurements to allow for source variability, microlensing-induced variability and systematic calibration offsets. Although the photometry will be blended with light from the lensing galaxy, the quasar point-source emission strongly dominates the emission. This is evident from the available ultra-violet–infrared imaging with the Hubble Space Telescope (e.g. Kochanek et al. 1999). The host galaxy emission can be fit in only a few cases, for most only accretion disc and torus components are constrained. We find some minor underfitting

which may be due to intrinsic reddening of the empirical templates (e.g. RX J0911+0551) or microlensing of the lensed quasar emission.

Following Calistro Rivera et al. (2021), we calculate the bolometric AGN luminosity (L_{AGN}) by integrating the quasar accretion disc model (‘big blue bump’) in the range 0.05–1 μm with an additive correction of 0.3 dex to account for X-ray emission not included in the model fit, i.e.

$$\log L_{\text{AGN}} = \log L_{0.05-1\mu\text{m}} + 0.3 - \log \mu_{\text{qso}}, \quad (1)$$

where μ_{qso} is the quasar magnification. We assume black hole mass (M_{BH}) estimates from the literature that were derived using the virial method. For consistency, we adopt the same quasar lensing magnification used for the black hole mass to infer the intrinsic bolometric AGN luminosity. For SDSS J1330+1810, the ionic or Balmer line widths have not been reported, so we infer a lower limit the black hole mass from the AGN bolometric luminosity assuming Eddington-limited accretion.

Plots of the IR–UV SED fitting is shown in Fig. A12 of the Appendix.

3.3 Star formation rates

Where possible, we obtain far-infrared luminosities from the literature. While AGNFITTER includes templates to fit the host galaxy dust emission, these models are empirically derived from low-redshift starbursts and may not be appropriate for high-redshift quasar hosts. Indeed, we found that the far-infrared–mm spectra are often poorly fit by these templates. Instead, we adopt far-infrared luminosities taken from the literature, most of which were calculated with modified black-body models, where the effective dust temperature and dust emissivity may be free parameters. Where there is insufficient photometry to fit a dust model, we assume an optically-thin modified black-body with the median effective dust temperature and emissivity found for a large sample of quasar hosts (Stacey et al. 2018). While the effective dust temperature may be quite different depending on the choice of model, the integrated luminosity will be similar as it is constrained by the photometry.

We convert far-infrared luminosity (40–120 μm) to total infrared luminosity (8–1000 μm) using the colour-correction factor (Dale et al. 2001) of 1.91 and to a dust-obscured SFR using a standard calibration (Kennicutt 1998) assuming a Salpeter initial mass function. While it has been proposed that the SFRs of AGN-starbursts may be overestimated due to an unconstrained contribution from AGN-heated dust, radiative transfer modelling of far-infrared lines from the most star-forming objects in the sample still support the existence of high star formation rate densities in combination with AGN heating (van der Werf et al. 2011; Li et al. 2020; Wang et al. 2019; Uzgil et al. 2016).

The intrinsic SFR for some of the lensed sources have previously been inferred from lens modelling of ALMA observations of sub-mm dust emission (Stacey et al. 2021). For APM 08279+5255, we adopt the CO magnification factor from lens modelling in the literature to infer a SFR from the uncorrected measurement (Riechers et al. 2009). All values and references are given in Table B2 of the Appendix.

Note that the sub-mm magnification is not the same as the quasar magnification, as these will be lensed differently depending on the size and location of the emitting region. We did not check for consistency between the lens models used to obtain black hole masses and those used to obtain the SFR, but these two properties are not directly compared here.

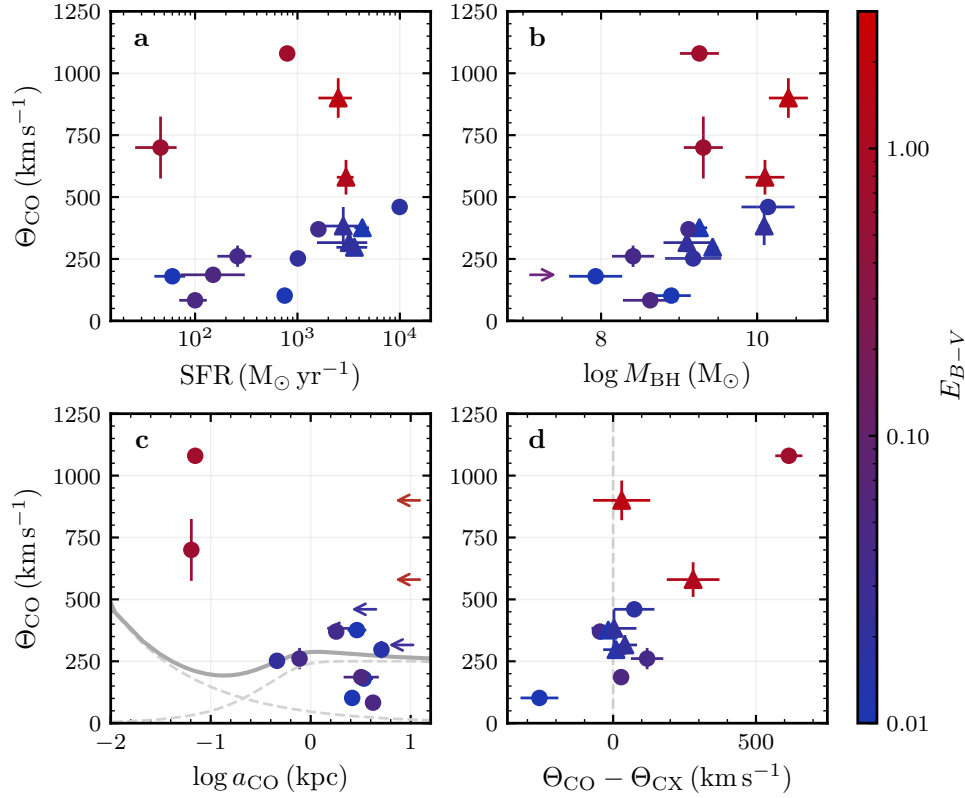


Figure 3. Comparison of CO line widths of the sample with reddening and various galaxy properties. **a:** $J_{\text{up}} > 7$ CO line width against SFR (lensing-corrected). **b:** CO line width against M_{BH} (lensing-corrected). **c:** FWHM of the physical size² of the CO emission (a_{CO} , i.e. twice the effective radius) against CO velocity line width. Twice the effective radius is often assumed to calculate dynamical mass of a disc (Förster Schreiber et al. 2018; Neeleman et al. 2021). The grey curves show a Keplerian rotation curve for a $10^{9.3} M_{\odot}$ black hole (the black hole masses of the two red quasars shown in this figure) and a rotation curve with peak velocity 500 km s^{-1} and transition radius of 500 pc adopted from fast-rotating massive galaxies at $z \approx 4.5$ (Fraternali et al. 2021), both inclined at 45 deg. **d:** The difference between the line width of the high-J CO line and the line width of a bulk gas tracer ([CII], CO (3–2) or [CI]). The circles identify the sources that are lensed. The colour scale indicates quasar extinction (E_{B-V}). The red quasars inhabit a different parameter space than the blue quasars across all indicators, while the blue quasars follow expected trends with dynamical mass and/or stellar feedback.

4 EVIDENCE FOR MOLECULAR OUTFLOWS

Details of the line properties, SFR, M_{BH} , E_{B-V} , $L_{0.05-1\mu\text{m}}$, adopted quasar magnifications and literature references for the sample of quasars is presented in Table B2 of the Appendix. The sample probes 2, 3 and 4 orders of magnitude in SFR, black hole mass and AGN luminosity, respectively.

The sample consists of a range of CO rotational transitions, $J_{\text{up}} = 7-11$. Previous studies of CO lines from quasar hosts have found generally consistent line widths for these high-excitation CO transitions relative to mid-J and low-J CO lines (Weiß et al. 2007; Li et al. 2020), although their kinematics have not yet been systematically studied at high redshift so little is previously known about their typical dynamics. We compare the CO (7–6) and CO (11–10)² line widths for MG J0414+0534 and find comparably large values of $\approx 1000 \text{ km s}^{-1}$. As shown in Fig. 2, these lines are significantly broader than the CO (3–2) line from the same system, suggesting that the CO (7–6) and CO (11–10) both probe dynamics that are different from the CO (3–2).

For the blue quasars, we find positive correlations between CO line width and SFR ($p = 0.002$) and between CO line width and black

hole mass ($p = 0.03$) with the Pearson correlation test. Such correlations can be explained by well-understood physical phenomena. The correlation with SFR (Fig. 3a) could reflect increased turbulence due to radiative stellar winds or supernovae: gas dispersion of up to 100 km s^{-1} can be induced by stellar feedback in regions of Eddington-limited star formation (Narayanan & Krumholz 2014; Hung et al. 2019) (note that if the SFRs are overestimated due to a contribution from AGN-heating (Kirkpatrick et al. 2015), the induced turbulence may be lower). Alternatively, it may reflect the relationship between SFR and dynamical mass. The correlation between line width and black hole mass (Fig. 3b) may reflect a larger dynamical mass as expected from canonical scaling relations between black hole mass and stellar mass (Ferrarese & Merritt 2000). These are expected correlations found for [CII] in quasar host galaxies (Neeleman et al. 2021), although these correlations have not been previously investigated for high-excitation CO lines. The red quasars do not follow the correlations observed by the blue quasars and there appears to be no significant correlation between SFR or black hole mass and reddening ($p = 0.45$ and $p = 0.24$, respectively, for the whole sample) in agreement with previous work (Calistro Rivera et al. 2021), although the red quasars in the sample have larger black holes on average.

In Fig. 3c, we compare the resolved size of the high-J CO line emission to the line width to determine whether these velocities could be produced by the dynamical mass of the galaxy. We find that the size of the emission from the blue quasars is $\sim 1 \text{ kpc}$, consistent

² If a system is modelling by multiple Gaussian sources, the size is a flux-weighted average

² The CO (11–10) line is used for MG J0414+0534 in all plots

with gas that could be from within a massive disc. For the two red quasars with resolved high-J CO line emission, the sizes of ≈ 70 pc would suggest an unfeasibly large enclosed mass of $\sim 10^{10} M_{\odot}$. This could be reconciled for J1042+1641 if the CO emission was from a Keplerian disc seen edge-on, although this is not consistent with the Gaussian shape of the line profile.

We also compare the high-excitation CO with [CII], CO (3–2) or [CI] line profiles to further test whether the line is associated with the bulk gas dynamics. [CII], CO (3–2), [CI] (1–0) and [CI] (2–1) trace the bulk of gas at lower temperatures and densities, so they are expected to probe a galaxy at larger disc radii (i.e. maximum circular velocity; e.g. Banerji et al. 2021; Fraternali et al. 2021). Fig. 3d shows the CO line width compared to the difference between the CO line width and the line width of a bulk gas tracer³, for the sources with such measurements. The difference is around zero or less for the blue quasars, so these lines could both relate to gas in the host galaxy. However, two out of three red quasars have CO line widths larger than their bulk gas line widths. This is not a clean test of the high-J CO dynamics as the kinematics and physical conditions of [CII], CO (3–2) and [CI] (2–1) lines are not systematically studied for quasar hosts (in particular, [CI] (2–1) may also be produced by cosmic ray excitation of molecular gas by AGN radiation), but larger velocities of high-J CO lines is difficult to explain from a radiative transfer perspective if they are co-spatial.

Both the lack of relationship with SFR and the compact size of the CO emission that is coincident with the quasar disfavour these being star-formation-driven outflows, and are contrary to findings of outflows from high-redshift star-forming galaxies (Ginolfi et al. 2020). Furthermore, if the broad high-J CO lines are driven by intense star formation, we should also expect to see outflows from blue quasars which are hosted in galaxies with Eddington-limited star formation rate densities, which we do not.

In summary, we conclude that quasar-driven outflows are the most likely explanation for the high-J CO linewidths of red quasars based on the following of evidence:

- (i) the lack of relationship with star formation rate;
- (ii) the lack of relationship with black hole mass (stellar mass);
- (iii) the larger velocities than lines that commonly probe the bulk of the gas in the galaxy for 2/3 red quasars; and
- (iv) the sizes of the line emission for the two red quasars where the high-J CO can be resolved that imply an unfeasibly large dynamical mass.

Using an orthogonal distance regression, we fit a linear relationship between CO line width and SFR for the blue quasars, as this shows a statistically significant correlation and the contribution of outflows to the lines tracing the bulk gas for individual red quasars is unknown. Assuming the line profiles have contributions from both outflows and host galaxy that can be described by Gaussians of equal height, we estimate line-of-sight outflow velocities of 500–1000 km s^{-1} . These velocities may be intrinsically larger depending on the geometry of the outflows. More accurate estimates of the outflow velocities will require detailed follow-up observations.

As we show in Figs. 4 and 5, there is no indication that the red quasars in our sample have larger AGN luminosities or larger Eddington ratios than the blue quasars, consistent with previous work by Calistro Rivera et al. (2021) but in contrast to Kim et al. (2015).

³ Our order of preference is [CII], CO (3–2) and [CI] (2–1), based on the relative prevalence of previous studies of the dynamics of the lines.

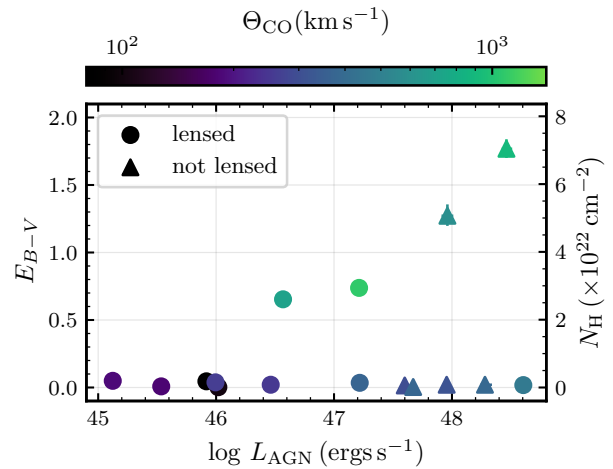


Figure 4. Reddening against bolometric AGN luminosity (lensing-corrected) coloured by high-J CO line width. The opposing y-axis shows the corresponding column density (Genzel et al. 2013). Circles identify sources that are lensed.

5 OUTFLOW DRIVING MECHANISM

5.1 Radiation pressure

Recent radiation-hydrodynamic simulations (Bieri et al. 2017; Costa et al. 2018a,b) predict that radiation pressure operates and launches outflows from < 1 kpc scales, thereby reducing the supply of gas for star formation in the inner region of the galaxy. This blow-out phase is likely short-lived because outflows propagate on a characteristic timescale of

$$t_{\text{out}} \sim 1 (R_{\text{out}}/\text{kpc}) (v_{\text{out}}/1000 \text{ km s}^{-1})^{-1} \text{ Myr.} \quad (2)$$

For this reason, we expect quasars to be below the effective Eddington limit unless their host galaxies are experiencing a powerful outflow. This limit creates a ‘forbidden zone’ on the column density (N_{H}) – Eddington ratio (λ_{Edd}) plane in the regime where the dust is optically thick to ultra-violet radiation which can be approximated by

$$N_{\text{H}} \sim \frac{\lambda_{\text{Edd}}/\sigma_{\text{T}}}{1 - \frac{\kappa_{\text{IR}}}{\kappa_{\text{T}}} \lambda_{\text{Edd}}}, \quad (3)$$

where σ_{T} is the Thomson cross-section, κ_{T} is the electron scattering opacity and κ_{IR} is the dust opacity (Ishibashi et al. 2018). Previous studies (Fabian et al. 2009; Ishibashi et al. 2018) have defined lower limits for the forbidden zone of $10^{21.5} - 10^{22} \text{ cm}^{-2}$ where column densities could be associated with diffuse cold gas in the galaxy: we have adopted the more conservative assumption of 10^{22} cm^{-2} , although the choice does not affect our interpretation.

We convert the $E_{\text{B-V}}$ from our SED fitting to a gas column density using the relationship found for a $z = 1.5$ star-forming galaxy by Genzel et al. (2013), assuming that the molecular gas column density is a good approximation for the total gas column density. Our SED fitting uncertainties suggest we cannot constrain $E_{\text{B-V}}$ at values below 0.01, so adopt this as an upper limit for the equivalent column density. As shown in Figs. 5 and 6, all four red quasars lie in the forbidden zone, suggesting that radiation pressure is responsible for these outflows. In contrast, the blue quasars populate a region of the parameter space where the nucleus is unobscured suggesting that they have already driven out their surrounding gas, consistent with the lack of a high velocity molecular gas component.

Two red quasars in our sample have measured sizes of their CO

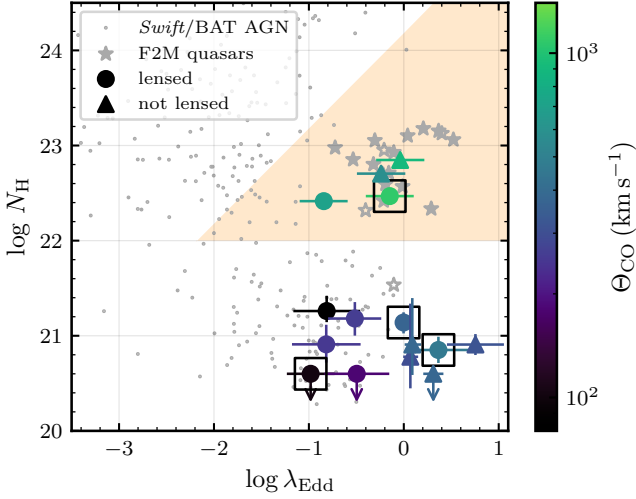


Figure 5. Quasar sample relative to the forbidden zone where radiation pressure on dust is sufficient to expel the obscuring column density. The shaded region identifies the ‘forbidden zone’ where quasars are expected to be in a short-lived blow-out phase (Ishibashi et al. 2018). The red quasars are in the forbidden zone where radiation pressure on dust can drive out the obscuring gas, indicating that radiation pressure is responsible for the outflows. Coloured symbols indicate the objects in this work, coloured according to their $J \geq 7$ CO line width. Boxes identify the objects in our sample with UV/X-ray ultra-fast outflows or broad absorption lines (Chartas 2000). The stars show quasars from F2M surveys ($0.1 < E_{B-V} < 2.5$; Glikman et al. 2012) where N_H is inferred from E_{B-V} (filled stars) or X-ray spectra (open stars) (Glikman 2017). The dots are X-ray detected AGN in the *Swift*/BAT sample (Ricci et al. 2017), where N_H is inferred from X-ray spectra.

emission from lens modelling in this work (Figs. A5 and A8). From Eq. 2 and the estimated outflow contribution, we estimate an outflow timescale of ≈ 0.1 Myr for MG J0414+0534 and J1042+1641. This is within the expected timescale of a radiatively-driven blow-out (Ishibashi et al. 2017, 2018).

5.2 Testing an energy-driven scenario

Fig. 5 supports the scenario that radiation pressure drives the observed outflows. However, outflows may also be ‘energy-driven’ by high-velocity winds produced near the accretion disc (King 2010; Faucher-Giguère & Quataert 2012; Costa et al. 2014, 2020). Ultra-fast outflows have been detected in X-ray spectra of high-redshift quasars (Chartas et al. 2021) including the red quasar MG J0414+0534, which contains an ultra-fast outflow with velocity $0.3c$ (Dadina et al. 2018) that could potentially power the observed molecular outflow. The kinematics of the wind is a key factor to discriminate between the two scenarios: the momentum flux for an energy-driven outflow is expected to be

$$\dot{p}_{\text{out}} \sim \frac{v_{\text{UFO}} L_{\text{AGN}}}{v_{\text{out}} c}, \quad (4)$$

where v_{out} and v_{UFO} are the velocities of the molecular outflow and ultra-fast outflow, respectively (Costa et al. 2018b). For the inferred $L_{\text{AGN}} = 10^{47.2}$ ergs s^{-1} , we predict an energy-driven mass outflow rate ($\dot{M} = \dot{p}/v_{\text{out}}$) of $\approx 10^6 M_{\odot} \text{ yr}^{-1}$ for the gas probed by the CO(11–10). Adopting a simple spherical model for the molecular outflow with radius of 70 pc and velocity 1000 km s^{-1} , the implied outflow timescale is ≈ 0.07 Myr and thus the total outflowing mass is $\approx 10^{10} M_{\odot}$. The CO(1–0) line is commonly used to probe the bulk

molecular gas mass in galaxies in the high-redshift Universe, assuming a CO-to- H_2 conversion factor: adopting the 3σ upper limit for the non-detection of CO(1–0) (Sharon et al. 2016), a typical (Greve et al. 2014) conversion factor of $0.8 \text{ K km s}^{-1} \text{ pc}^2$ and magnification factor of 10 (Stacey et al. 2018), we estimate the molecular gas mass in the host galaxy is $< 10^{9.5} M_{\odot}$. Therefore, for an energy-driven wind model, the gas in the outflow from MG J0414+0534 would be more than twice as massive as the molecular gas in the disc: an unlikely scenario given the high SFR (Table B2) and the massive molecular gas reservoirs of quasar hosts that are similar to normal starbursts (Riechers 2011; Riechers et al. 2011; Sharon et al. 2016). This disfavours an energy-driven scenario for this object, requiring that an accretion disc wind must couple very inefficiently with the ISM in order to produce the outflow we observe.

In Fig. 5, we identify the quasars in our sample where ultra-fast outflows or broad absorption lines have been detected in UV or X-ray spectra. Three out of four quasars that have such features do not show evidence for high-velocity molecular gas, suggesting that radiation pressure on dust is a better predictor of the presence of molecular outflows.

6 CONCLUSIONS

It has frequently been suggested that strong quasar reddening is related to a transitional ‘blow-out’ phase in which quasars evacuate the obscuring gas in the nuclear region (e.g. Glikman et al. 2012; Glikman 2017; Banerji et al. 2012; Calistro Rivera et al. 2021). Here, we find evidence for a direct connection between quasar dust-obscuration and molecular outflows. This phenomenon is predicted by theoretical models of radiation pressure on dust and is in agreement with observational evidence for fundamentally different properties of red quasars. Our results indicate that a radiatively-driven blow-out could be a viable mechanism to produce the rapid quenching of star formation (Belli et al. 2021; Williams et al. 2021) and depleted molecular gas reservoirs (Whitaker et al. 2021) recently observed in quiescent galaxies at cosmic noon.

In addition, we introduce a new approach to identifying molecular outflows through high-excitation CO lines. Previously, much sought-after cold outflows have typically been identified from offsets from the systemic velocity (which is often ill-defined for quasars) and broad wings of [CII] lines (which may be atomic or ionised gas), while we find neither here. The dearth of detection of cold outflows has led to speculation that molecules are destroyed in more energetic systems such that the outflowing gas is primarily ionised (Fiore et al. 2017). Our results show that molecules can survive in outflows, even from the brightest quasars ($L_{\text{AGN}} > 10^{48}$ ergs s^{-1}). These outflows have velocities comparable to the maximum outflow velocities of ionised gas for quasars with $L_{\text{AGN}} \sim 10^{47} - 10^{48}$ ergs s^{-1} (Fiore et al. 2017). This suggests that the molecular outflow velocities are maintained as the outflow expands out of the galaxy (~ 10 kpc) where the cold outflow may either stall or be destroyed, transitioning to a purely ionised phase, as predicted by radiation-hydrodynamical simulations (Costa et al. 2018a,b).

Future investigations will involve other gas tracers to determine the multi-phase properties of gas in these outflows. Such data could be used to estimate the outflow mass, which requires an understanding of the physical conditions of the outflowing gas. Additionally, the

⁴ Note that this would be a factor of 2 lower if we assume the dust magnification in Table B1

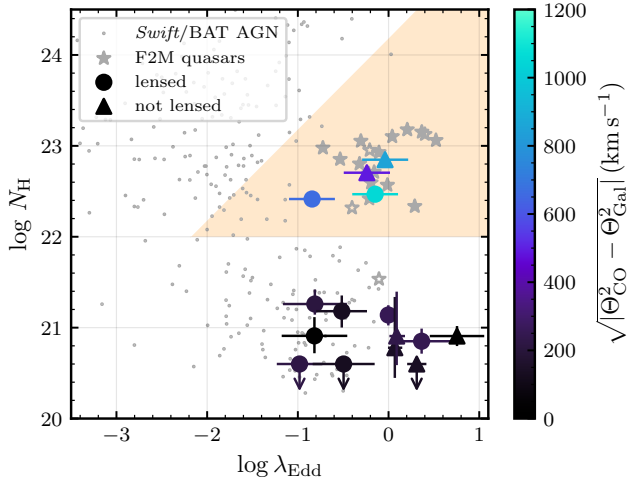


Figure 6. Quasar sample relative to the forbidden zone where radiation pressure on dust is sufficient to expel the obscuring column density. Same as Fig. 5 but with the colours indicating the estimated outflow contribution (see Section 4).

CO emission has been resolved for all of the lensed quasar systems in the data reported here and for most of the sample (Stacey & McKean 2018; Stacey et al. 2021): by taking advantage of lensing magnification, gravitational lens modelling (e.g. Stacey et al. 2021; Rizzo et al. 2021) of higher quality data could allow us to reconstruct the CO emission and diagnose the outflow kinetics.

Although the difference in reddening and CO line width is striking, our work here involves only four quasars with $E_{B-V} > 0.1$. Future work would particularly benefit from a systematic study of a larger sample to follow the evolution of quasars via the relationship between CO velocity, quasar obscuration, Eddington ratio and star formation rate. Such studies will be important to constrain the life-cycles of AGN and their role in shaping the evolution of massive galaxies.

ACKNOWLEDGEMENTS

The authors thank the anonymous referee, Adam Schaefer, Simon White and Volker Springel for helpful discussions, and Michael Bremer for help with the NOEMA data reduction. HRS acknowledges funding from the European Research Council (ERC) under the European Union’s Horizon 2020 research and innovation programme (LEDA: grant agreement No 758853). This research used SciPy, NumPy and Matplotlib packages for Python (Virtanen et al. 2020; Harris et al. 2020; Hunter 2007), and also the NASA/IPAC Extragalactic Database (NED), SIMBAD (Wenger et al. 2000) and VizieR (DOI : 10.26093/cds/vizieR) catalogue access tools. We made use of ALMA data with project codes 2018.1.01008.S, 2019.1.00948.S and 2019.1.00964.S. ALMA is a partnership of ESO (representing its member states), NSF (USA) and NINS (Japan), together with NRC (Canada), MOST and ASIAA (Taiwan), and KASI (Republic of Korea), in cooperation with the Republic of Chile. The Joint ALMA Observatory is operated by ESO, AUI/NRAO and NAOJ. We also used observations carried out under project number S17BV [001] with the IRAM NOEMA Interferometer. IRAM is supported by INSU/CNRS (France), MPG (Germany) and IGN (Spain).

DATA AVAILABILITY

All observations reported in this work are publicly available in the ALMA archive (<https://almascience.eso.org/aq>) or IRAM Data Archive (<https://www.iram-institute.org/EN/content-page-386-7-386-0-0-0.html>) and all the analysis was performed with publicly available software. The data sets generated during the current study are available from the corresponding author upon reasonable request.

References

- Agnello A., et al., 2017, *MNRAS*, 472, 4038
 Antonucci R., 1993, *ARA&A*, 31, 473
 Banerji M., McMahon R. G., Hewett P. C., Alaghband-Zadeh S., Gonzalez-Solares E., Venemans B. P., Hawthorn M. J., 2012, *MNRAS*, 427, 2275
 Banerji M., Alaghband-Zadeh S., Hewett P. C., McMahon R. G., 2015, *MNRAS*, 447, 3368
 Banerji M., Carilli C. L., Jones G., Wagg J., McMahon R. G., Hewett P. C., Alaghband-Zadeh S., Feruglio C., 2017, *MNRAS*, 465, 4390
 Banerji M., Jones G. C., Wagg J., Carilli C. L., Bisbas T. G., Hewett P. C., 2018, *MNRAS*, 479, 1154
 Banerji M., Jones G. C., Carniani S., DeGraf C., Wagg J., 2021, *MNRAS*, 503, 5583
 Barvainis R., Maloney P., Antonucci R., Alloin D., 1997, *ApJ*, 484, 695
 Barvainis R., Alloin D., Guilloteau S., Antonucci R., 1998, *ApJ*, 492, L13
 Bate N. F., et al., 2018, *MNRAS*, 479, 4796
 Belli S., et al., 2021, *ApJ*, 909, L11
 Bieri R., Dubois Y., Rosdahl J., Wagner A., Silk J., Mamon G. A., 2017, *MNRAS*, 464, 1854
 Bischetti M., Maiolino R., Carniani S., Fiore F., Piconcelli E., Fluetsch A., 2019, *A&A*, 630, A59
 Blackburne J. A., Pooley D., Rappaport S., Schechter P. L., 2011, *ApJ*, 729, 34
 Calistro Rivera G., Lusso E., Hennawi J. F., Hogg D. W., 2016, *ApJ*, 833, 98
 Calistro Rivera G., et al., 2021, *A&A*, 649, A102
 Carilli C. L., Riechers D., Walter F., Maiolino R., Wagg J., Lentati L., McMahon R., Wolfe A., 2013, *ApJ*, 763, 120
 Carniani S., et al., 2013, *A&A*, 559, A29
 Carniani S., et al., 2019, *MNRAS*, 489, 3939
 Chartas G., 2000, *ApJ*, 531, 81
 Chartas G., et al., 2021, *ApJ*, 920, 24
 Cicone C., et al., 2021, *A&A*, 654, L8
 Cornachione M. A., Morgan C. W., Millon M., Bentz M. C., Courbin F., Bonvin V., Falco E. E., 2020, *ApJ*, 895, 125
 Costa T., Sijacki D., Haehnelt M. G., 2014, *MNRAS*, 444, 2355
 Costa T., Rosdahl J., Sijacki D., Haehnelt M. G., 2018a, *MNRAS*, 473, 4197
 Costa T., Rosdahl J., Sijacki D., Haehnelt M. G., 2018b, *MNRAS*, 479, 2079
 Costa T., Pakmor R., Springel V., 2020, *MNRAS*, 497, 5229
 Dadina M., et al., 2018, *A&A*, 610, L13
 Dale D. A., Helou G., Contursi A., Silbermann N. A., Kolhatkar S., 2001, *ApJ*, 549, 215
 Di Matteo T., Springel V., Hernquist L., 2005, *Nature*, 433, 604
 Dubois Y., et al., 2021, *A&A*, 651, A109
 Fabian A. C., 1999, *MNRAS*, 308, L39
 Fabian A. C., 2012, *ARA&A*, 50, 455
 Fabian A. C., Vasudevan R. V., Gandhi P., 2008, *MNRAS*, 385, L43
 Fabian A. C., Vasudevan R. V., Mushotzky R. F., Winter L. M., Reynolds C. S., 2009, *MNRAS*, 394, L89
 Faucher-Giguère C.-A., Quataert E., 2012, *MNRAS*, 425, 605
 Fawcett V. A., Alexander D. M., Rosario D. J., Klindt L., Fotopoulou S., Lusso E., Morabito L. K., Calistro Rivera G., 2020, *MNRAS*, 494, 4802
 Ferrarese L., Merritt D., 2000, *ApJ*, 539, L9
 Feruglio C., et al., 2018, *A&A*, 619, A39
 Fiore F., et al., 2017, *A&A*, 601, A143
 Förster Schreiber N. M., Wuyts S., 2020, *ARA&A*, 58, 661

- Förster Schreiber N. M., et al., 2018, *ApJS*, **238**, 21
- Fraternali F., Karim A., Magnelli B., Gómez-Guijarro C., Jiménez-Andrade E. F., Poses A. C., 2021, *A&A*, **647**, A194
- Fukumura K., Kazanas D., Shrader C., Behar E., Tombesi F., Contopoulos I., 2018, *ApJ*, **864**, L27
- Gallerani S., et al., 2017, *MNRAS*, **467**, 3590
- Genzel R., et al., 2013, *ApJ*, **773**, 68
- Ginolfi M., et al., 2020, *A&A*, **633**, A90
- Glikman E., 2017, *Research Notes of the American Astronomical Society*, **1**, 48
- Glikman E., et al., 2012, *ApJ*, **757**, 51
- Glikman E., Simmons B., Mailly M., Schawinski K., Urry C. M., Lacy M., 2015, *ApJ*, **806**, 218
- Glikman E., Rusu C. E., Djorgovski S. G., Graham M. J., Stern D., Urrutia T., Lacy M., O’Meara J. M., 2018a, arXiv e-prints, p. [arXiv:1807.05434](https://arxiv.org/abs/1807.05434)
- Glikman E., et al., 2018b, *ApJ*, **861**, 37
- Greve T. R., et al., 2014, *ApJ*, **794**, 142
- Guilloteau S., Lucas R., 2000, in J. G. Mangum & S. J. E. Radford ed., *Astronomical Society of the Pacific Conference Series Vol. 217, Imaging at Radio through Submillimeter Wavelengths*. p. 299
- Harris C. R., et al., 2020, *Nature*, **585**, 357–362
- Harrison C. M., 2017, *Nature Astronomy*, **1**, 0165
- Harrison C. M., Costa T., Tadhunter C. N., Flütsch A., Kakkad D., Perna M., Vietri G., 2018, *Nature Astronomy*, **2**, 198
- Hezaveh Y. D., et al., 2013, *ApJ*, **767**, 132
- Hung C.-L., et al., 2019, *MNRAS*, **482**, 5125
- Hunter J. D., 2007, *Computing in Science & Engineering*, **9**, 90
- Hwang H.-C., Zakamska N. L., Alexandroff R. M., Hamann F., Greene J. E., Perrotta S., Richards G. T., 2018, *MNRAS*, **477**, 830
- Ishibashi W., Banerji M., Fabian A. C., 2017, *MNRAS*, **469**, 1496
- Ishibashi W., Fabian A. C., Ricci C., Cелotti A., 2018, *MNRAS*, **479**, 3335
- Kennicutt Jr. R. C., 1998, *ApJ*, **498**, 541
- Kim D., Im M., Glikman E., Woo J.-H., Urrutia T., 2015, *ApJ*, **812**, 66
- King A., 2005, *ApJ*, **635**, L121
- King A. R., 2010, *MNRAS*, **402**, 1516
- Kirkpatrick A., Pope A., Sajina A., Roebuck E., Yan L., Armus L., Díaz-Santos T., Stierwalt S., 2015, *ApJ*, **814**, 9
- Klindt L., Alexander D. M., Rosario D. J., Lusso E., Fotopoulou S., 2019, *MNRAS*, **488**, 3109
- Kochanek C. S., Falco E. E., Impey C., Lehar J., McLeod B., Rix H.-W., 1999, *The CASTLES Survey*, <https://www.cfa.harvard.edu/castles/>
- Leipski C., et al., 2013, *ApJ*, **772**, 103
- Li J., et al., 2020, *ApJ*, **889**, 162
- Liu G., Zakamska N. L., Greene J. E., Nesvadba N. P. H., Liu X., 2013, *MNRAS*, **430**, 2327
- McMullin J. P., Waters B., Schiebel D., Young W., Golap K., 2007, in Shaw R. A., Hill F., Bell D. J., eds, *Astronomical Society of the Pacific Conference Series Vol. 376, Astronomical Data Analysis Software and Systems XVI*. p. 127
- Monadi R., Bird S., 2022, *MNRAS*, **511**, 3501
- Morgan N. D., Caldwell J. A. R., Schechter P. L., Dressler A., Egami E., Rix H.-W., 2004, *AJ*, **127**, 2617
- Narayanan D., Krumholz M. R., 2014, *MNRAS*, **442**, 1411
- Neeleman M., et al., 2021, *ApJ*, **911**, 141
- Nomura M., Ohsuga K., 2017, *MNRAS*, **465**, 2873
- Novak M., et al., 2020, *ApJ*, **904**, 131
- Perrotta S., Hamann F., Zakamska N. L., Alexandroff R. M., Rupke D., Wylezalek D., 2019, *MNRAS*, **488**, 4126
- Planck Collaboration et al., 2016, *A&A*, **594**, A13
- Prevot M. L., Lequeux J., Maurice E., Prevot L., Rocca-Volmerange B., 1984, *A&A*, **132**, 389
- Raimundo S. I., Fabian A. C., Bauer F. E., Alexander D. M., Brandt W. N., Luo B., Vasudevan R. V., Xue Y. Q., 2010, *MNRAS*, **408**, 1714
- Ricci C., et al., 2017, *Nature*, **549**, 488
- Riechers D. A., 2011, *ApJ*, **730**, 108
- Riechers D. A., Walter F., Carilli C. L., Lewis G. F., 2009, *ApJ*, **690**, 463
- Riechers D. A., et al., 2011, *ApJ*, **739**, L32
- Rizzo F., Vegetti S., Fraternali F., Stacey H. R., Powell D., 2021, *MNRAS*, **507**, 3952
- Rosario D. J., Fawcett V. A., Klindt L., Alexander D. M., Morabito L. K., Fotopoulou S., Lusso E., Calistro Rivera G., 2020, *MNRAS*, **494**, 3061
- Rosario D. J., Alexander D. M., Moldon J., Klindt L., Thomson A. P., Morabito L., Fawcett V. A., Harrison C. M., 2021, *MNRAS*, **505**, 5283
- Roth N., Kasen D., Hopkins P. F., Quataert E., 2012, *ApJ*, **759**, 36
- Rupke D. S. N., Gültekin K., Veilleux S., 2017, *ApJ*, **850**, 40
- Salomé P., Guélin M., Downes D., Cox P., Guilloteau S., Omont A., Gavazzi R., Neri R., 2012, *A&A*, **545**, A57
- Schaye J., et al., 2015, *MNRAS*, **446**, 521
- Shajib A. J., et al., 2019, *MNRAS*, **483**, 5649
- Shajib A. J., et al., 2020, *MNRAS*, **494**, 6072
- Sharon C. E., Riechers D. A., Hodge J., Carilli C. L., Walter F., Weiß A., Knudsen K. K., Wagg J., 2016, *ApJ*, **827**, 18
- Sluse D., Hutsemékers D., Courbin F., Meylan G., Wambsgans J., 2012, *A&A*, **544**, A62
- Somerville R. S., Davé R., 2015, *ARA&A*, **53**, 51
- Spilker J. S., et al., 2016, *ApJ*, **826**, 112
- Stacey H. R., McKean J. P., 2018, *MNRAS*, **481**, L40
- Stacey H. R., et al., 2018, *MNRAS*, **476**, 5075
- Stacey H. R., Lafontaine A., McKean J. P., 2020, *MNRAS*, **493**, 5290
- Stacey H. R., et al., 2021, *MNRAS*, **500**, 3667
- Temple M. J., Banerji M., Hewett P. C., Coatman L., Maddox N., Peroux C., 2019, *MNRAS*, **487**, 2594
- Tuan-Anh P., Hoai D. T., Nhung P. T., Diep P. N., Phuong N. T., Thao N. T., Darriulat P., 2017, *MNRAS*, **467**, 3513
- Urrutia T., Becker R. H., White R. L., Glikman E., Lacy M., Hodge J., Gregg M. D., 2009, *ApJ*, **698**, 1095
- Urry C. M., Padovani P., 1995, *PASP*, **107**, 803
- Uzgil B. D., Bradford C. M., Hailey-Dunsheath S., Maloney P. R., Aguirre J. E., 2016, *ApJ*, **832**, 209
- Vayner A., et al., 2021, *MNRAS*, **504**, 4445
- Virtanen P., et al., 2020, *Nature Methods*, **17**, 261
- Wagg J., Wilner D. J., Neri R., Downes D., Wiklind T., 2006, *ApJ*, **651**, 46
- Walter F., Riechers D., Cox P., Neri R., Carilli C., Bertoldi F., Weiss A., Maiolino R., 2009, *Nature*, **457**, 699
- Wang F., Wang R., Fan X., Wu X.-B., Yang J., Neri R., Yue M., 2019, *ApJ*, **880**, 2
- Webster R. L., Francis P. J., Petersont B. A., Drinkwater M. J., Masci F. J., 1995, *Nature*, **375**, 469
- Weinberger R., et al., 2017, *MNRAS*, **465**, 3291
- Weiß A., Downes D., Neri R., Walter F., Henkel C., Wilner D. J., Wagg J., Wiklind T., 2007, *A&A*, **467**, 955
- Wenger M., et al., 2000, *A&AS*, **143**, 9
- Whitaker K. E., et al., 2021, *Nature*, **597**, 485
- Williams C. C., et al., 2021, *ApJ*, **908**, 54
- Wu X.-B., et al., 2015, *Nature*, **518**, 512
- Zakamska N. L., et al., 2019, *MNRAS*, **489**, 497
- van der Werf P. P., et al., 2010, *A&A*, **518**, L42
- van der Werf P. P., et al., 2011, *ApJ*, **741**, L38

APPENDIX A: SUPPORTING FIGURES

APPENDIX B: SUPPORTING TABLES

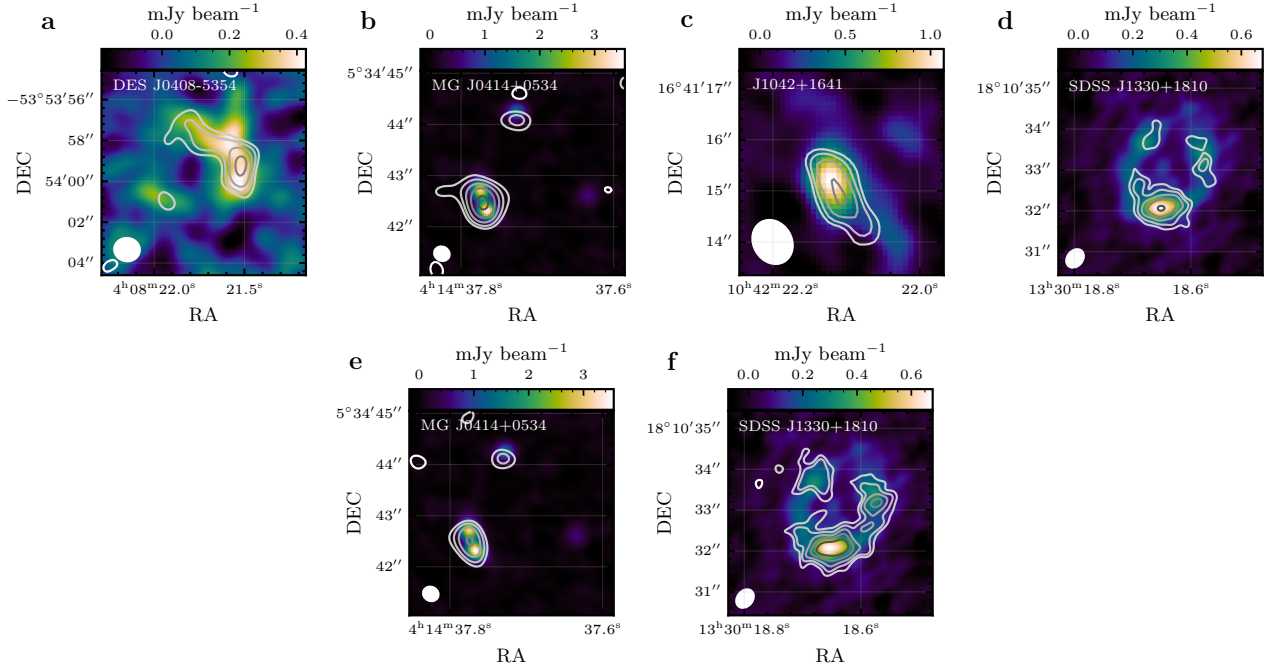


Figure A1. ALMA imaging for the new data presented in this work. **a–d**: the sub-mm continuum emission with contours of the velocity-integrated CO line emission in signal-to-noise intervals of $-3, 3, 3\sqrt{2}, 6, 6\sqrt{2}, \dots$ etc. The synthesised beam is shown by the ellipse in the lower-left corner. **e, f**: the same for the [CI] line emission.

Table B1. Summary of lens modelling in this work, using visILENS (Hezaveh et al. 2013; Spilker et al. 2016). We give the marginalised posteriors from the MCMC of the major axis (a), axis ratio (q), magnification (μ) for each Gaussian source component. The lens model parameters are kept fixed except the position of the lens, to account for any astrometric offsets. [‡] After removal of synchrotron emission, see text for details.

Name	Data	a_1 (arcsec)	a_1 (kpc)	q_1	μ_1	a_2 (arcsec)	a_2 (kpc)	q_2	μ_2	Lens model reference
MG J0414+0534	continuum [‡]	0.019 ± 0.001	0.16 ± 0.01	$\equiv 1$	29.6 ± 0.3	0.189 ± 0.005	1.56 ± 0.04	$\equiv 1$	15.4 ± 0.2	Stacey et al. (2020)
	CO (11–10)	0.009 ± 0.002	0.07 ± 0.02	$\equiv 1$	42 ± 5	-	-	-	-	
DES J0408–5354	continuum	0.30 ± 0.07	2.5 ± 0.6	$\equiv 1$	10 ± 1	0.14 ± 0.09	1.2 ± 0.8	$\equiv 1$	6 ± 4	Agnello et al. (2017)
	CO (7–6)	0.21 ± 0.02	1.8 ± 0.2	0.4 ± 0.1	18 ± 1	0.46 ± 0.04	3.8 ± 0.3	$\equiv 1$	5.1 ± 0.6	
	[CI] (2–1)	0.31 ± 0.02	2.6 ± 0.2	0.4 ± 0.1	14 ± 1	-	-	-	-	
J1042+1641	continuum	0.008 ± 0.002	0.07 ± 0.02	$\equiv 1$	49 ± 7	-	-	-	-	Glikman et al. (2018a)
	CO (10–9)	0.008 ± 0.001	0.07 ± 0.01	$\equiv 1$	43 ± 1	-	-	-	-	
SDSS J1330+1810	continuum	0.014 ± 0.003	0.12 ± 0.02	$\equiv 1$	26 ± 1	0.46 ± 0.02	4.0 ± 0.2	0.48 ± 0.03	6.8 ± 0.3	Shajib et al. (2019)
	CO (7–6)	0.014 ± 0.001	0.12 ± 0.01	$\equiv 1$	24 ± 1	0.44 ± 0.05	3.8 ± 0.4	0.7 ± 0.1	5.6 ± 0.3	
	[CI] (2–1)	0.014 ± 0.001	0.12 ± 0.01	$\equiv 1$	23 ± 1	0.34 ± 0.05	2.9 ± 0.4	0.8 ± 0.1	8.4 ± 0.8	

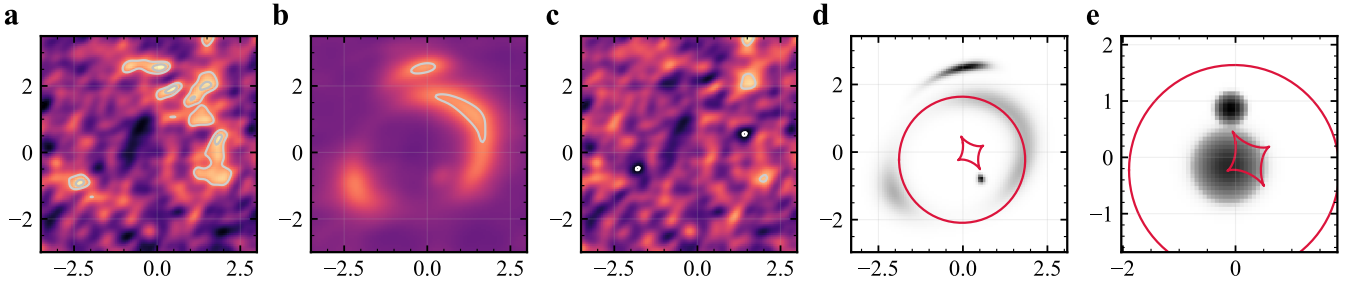


Figure A2. Lens modelling of DES J0408–5354 continuum. **a–c:** The dirty image of the data, dirty image of the model (with the same colour-scale as the data) and residual image. The contours are in signal-to-noise intervals of $-3, 3, 3\sqrt{2}, 6, 6\sqrt{2}, \dots$ etc. **d:** The lens model (grey; log-scale) and lensing caustics (red). **e** The source (grey; log-scale) and caustics (red). The scale is in arcsec relative to the phase centre of the observation.

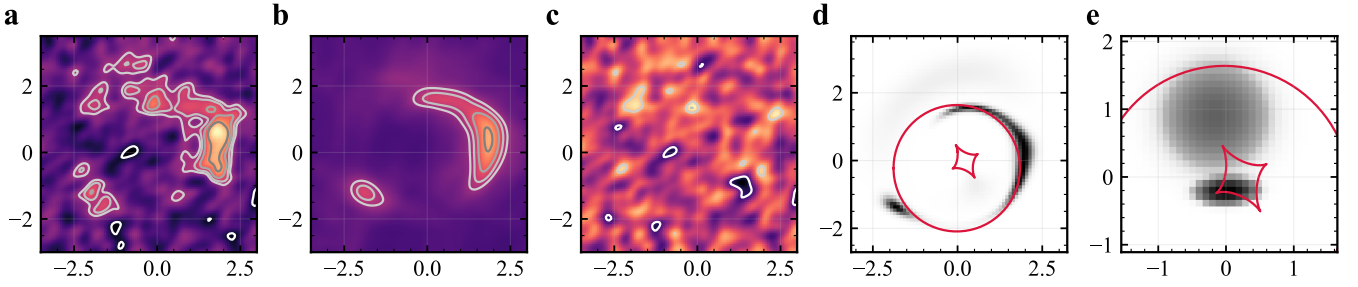


Figure A3. Lens modelling of DES J0408–5354 CO (7–6). Labels as in Fig. A2.

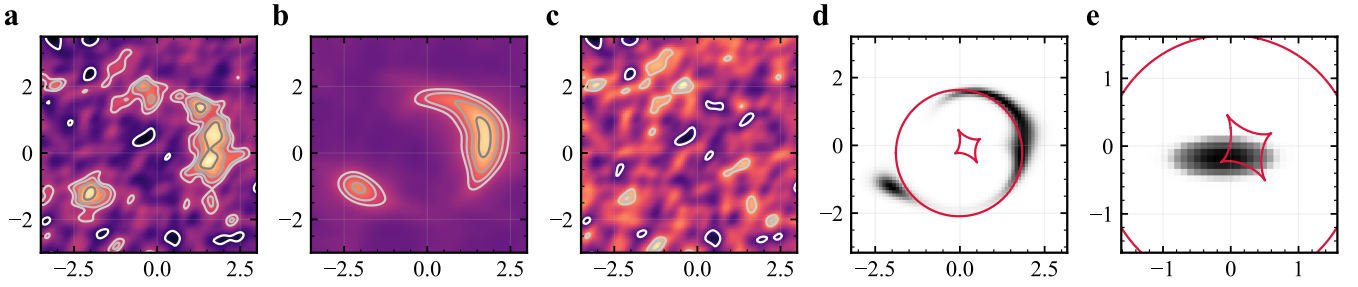


Figure A4. Lens modelling of DES J0408–5354 [CI] (2–1). Labels as in Fig. A2.

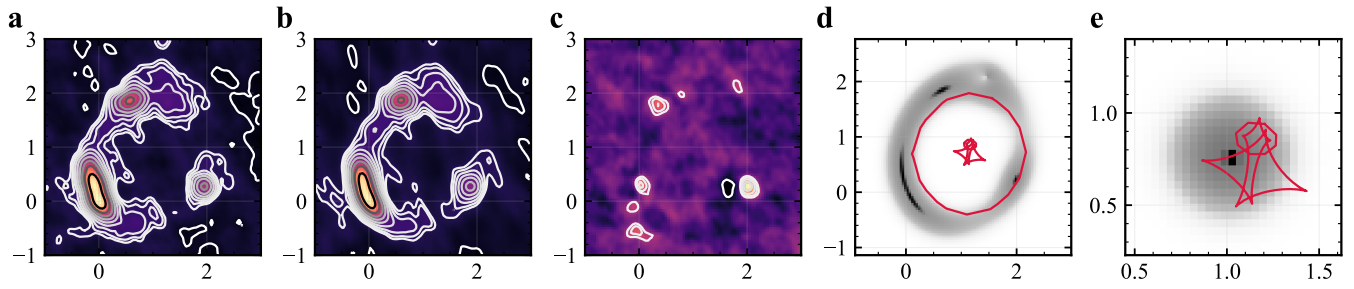


Figure A5. Lens modelling of MG J0414+0534 continuum. Labels as in Fig. A2. The synchrotron emission has been removed from the continuum (see text for explanation).

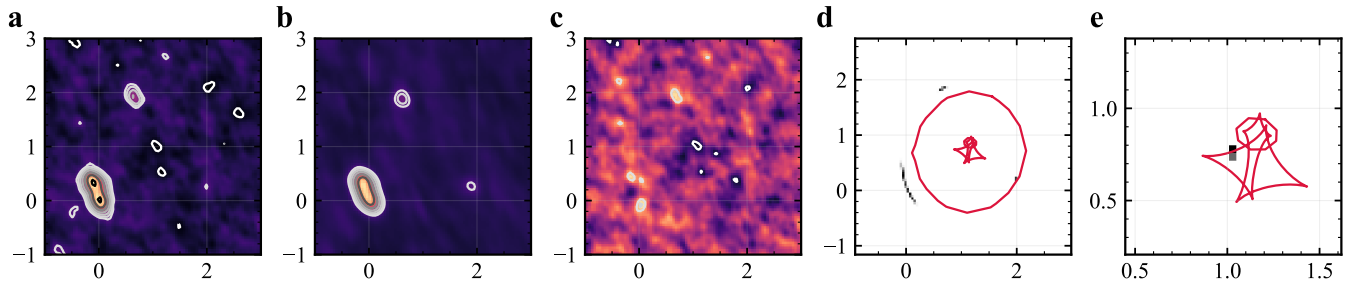


Figure A6. Lens modelling of MG J0414+0534 CO(11–10). Labels as in Fig. A3.

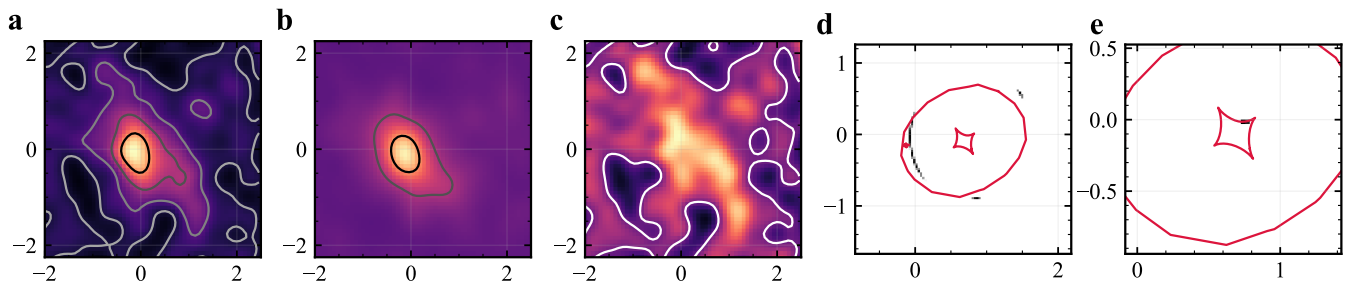


Figure A7. Lens modelling of J1042+1641 continuum. Labels as in Fig. A2.

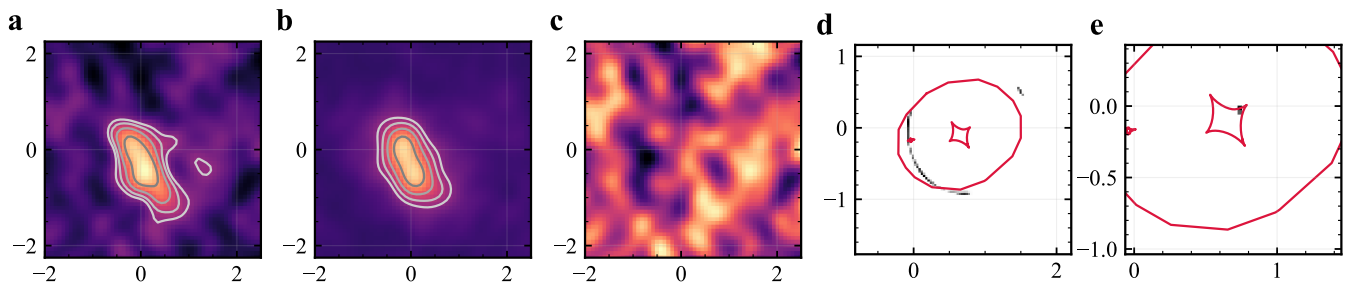


Figure A8. Lens modelling of J1042+1641 CO(10–9). Labels as in Fig. A2.

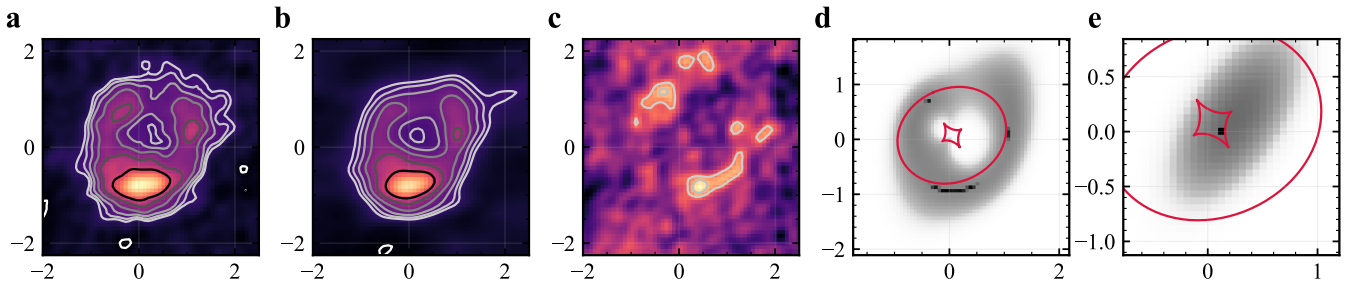


Figure A9. Lens modelling of SDSS J1330+1810 continuum. Labels as in Fig. A2.

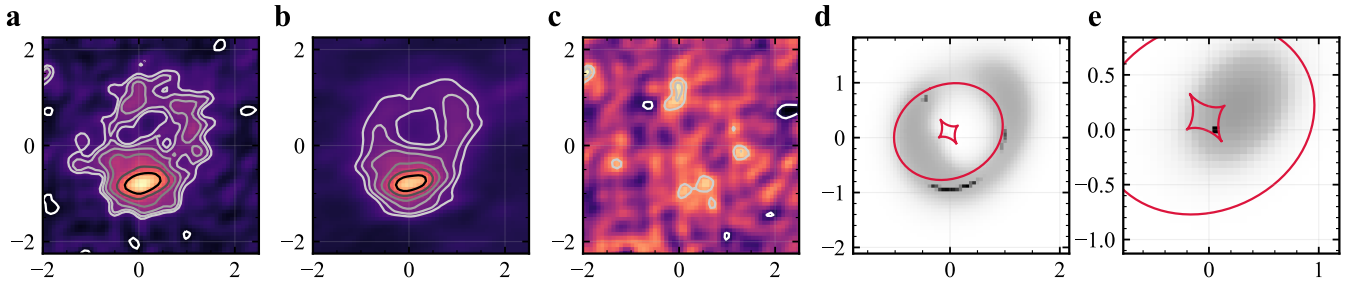


Figure A10. Lens modelling of SDSS J1330+1810 CO (7-6). Labels as in Fig. A2.

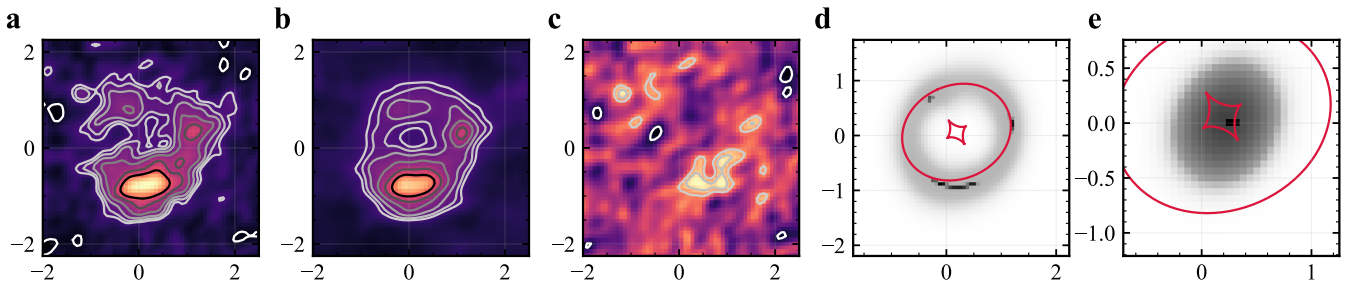


Figure A11. Lens modelling of SDSS J1330+1810 CI (2-1). Labels as in Fig. A2.

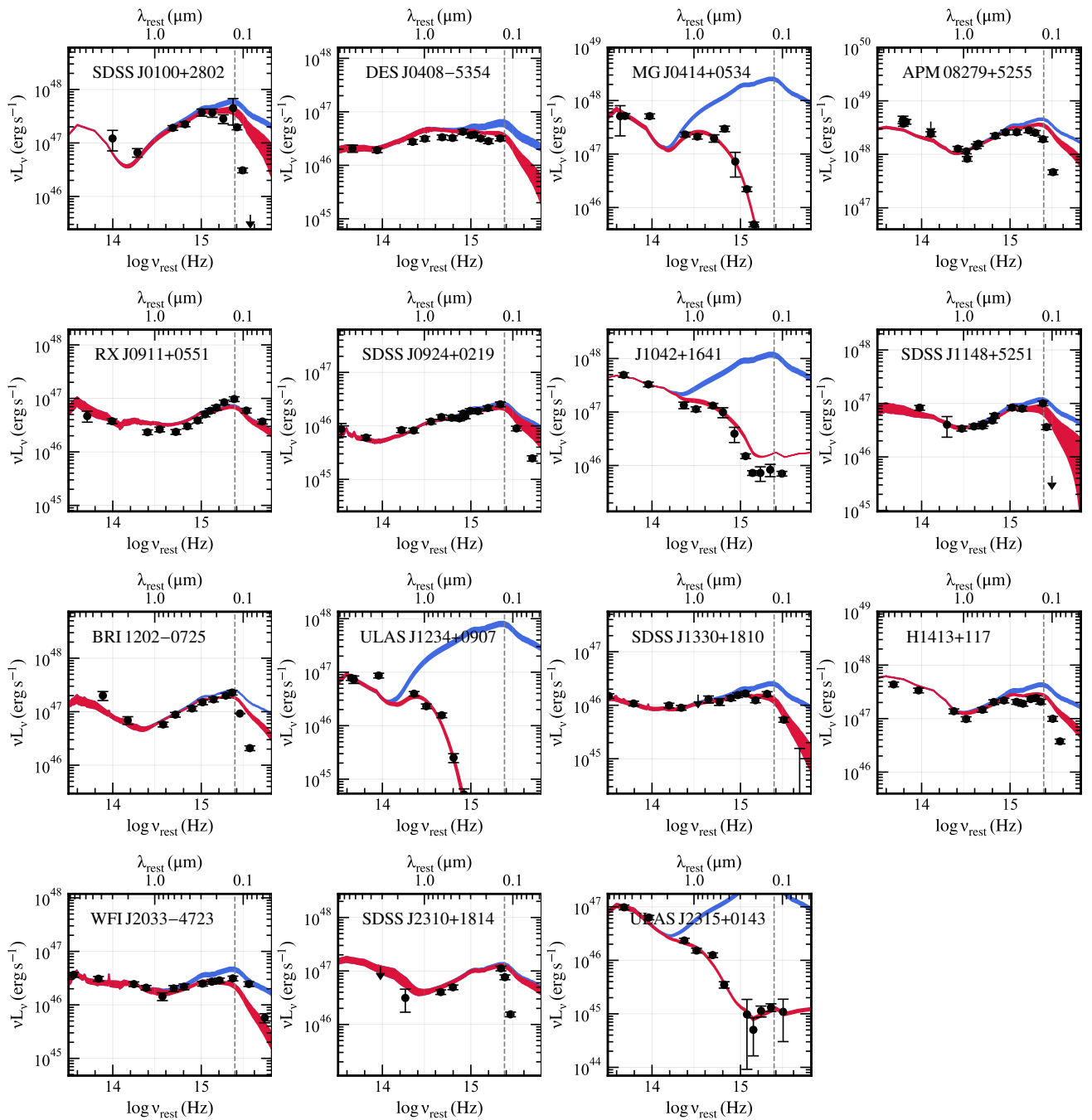


Figure A12. SED fits for the quasar sample. We use AGNFitter (Calistro Rivera et al. 2016) to fit broad-band SEDs from the ultra-violet to mid-infrared. The red curve is a solid fill between 16th to 86th percentiles of the models from the MCMC analysis. The blue curve shows the quasar models without dust attenuation. The grey dashed line is the rest-frame frequency of Lyman- α ; photometric measurements at or above this frequency are ignored because they are affected by absorption by the intergalactic medium.

Table B2. Summary of the objects in the sample. We give the number of lensed quasar images ($N_{\text{im}} = 1$ if not strongly lensed), source redshift (z_s), CO line transition (or other line), line FWHM from a single Gaussian fit to the line profile, SFR (lensing-corrected), black hole mass (M_{BH}), extinction (E_{B-V}), integrated luminosity of the accretion disc template ($\log L_{0.05-1\mu\text{m}}$, *not* lensing-corrected) and assumed value of the quasar magnification from the literature (μ_{qso}). Where no uncertainty was given for the black hole mass, we assume an uncertainty of 0.25 dex which is the typical scatter found for black hole scaling relations. If no uncertainty is given for the star formation rate, we assume it is only accurate to within a factor of 2. References given are for the line FWHM, black hole mass and quasar magnification, and photometry used for the optical–infrared SED fitting (if not from all-sky catalogues). * A fit to the CO FWHM was not reported for this line, but reported to be consistent with the [CII] FWHM.

Name	N_{im}	z_s	Line	Θ_{line} (km s^{-1})	SFR ($M_{\odot} \text{ yr}^{-1}$)	$\log M_{\text{BH}}$ (M_{\odot})	E_{B-V}	$\log L_{0.05-1\mu\text{m}}$ (ergs s^{-1})	μ_{qso}	References
DESJ0408–5354	4	2.375	CO (7–6)	260 ± 100	240^{+240}_{-120}	8.41 ± 0.27	$0.038^{+0.015}_{-0.016}$	$47.04^{+0.07}_{-0.08}$	22	Shajib et al. (2020), this work
			[CII] (2–1)	140 ± 40						This work
MG J0414+0534	4	2.64	CO (11–10)	1080 ± 20	800 ± 70	9.26	$0.738^{+0.017}_{-0.014}$	$48.66^{+0.04}_{-0.03}$	56.4	Blackburne et al. (2011); Stacey et al. (2018); Stacey & McKean (2018)
			CO (7–6)	1390 ± 240						This work
			[CII] (2–1)	500 ± 120						This work
			CO (3–2)	470 ± 40						This work
APM 08279+5255	4	3.91	CO (9–8)	460 ± 20	10000 ± 200	10.0	$0.018^{+0.006}_{-0.006}$	$48.91^{+0.01}_{-0.02}$	4	Weiß et al. (2007); Stacey et al. (2018)
			[CII] (1–0)	390 ± 70						Wagg et al. (2006)
RX J0911+0551	4	2.79	CO (11–10)	100 ± 30	750 ± 50	8.9	$0.002^{+0.005}_{-0.002}$	$47.10^{+0.02}_{-0.02}$	17.5	Blackburne et al. (2011); Stacey et al. (2021); Tuan-Anh et al. (2017)
			CO (3–2)	360 ± 60						Tuan-Anh et al. (2017)
SDSS J0924+0219	4	1.525	CO (8–7)	180 ± 10	60 ± 20	7.93 ± 0.35	$0.008^{+0.012}_{-0.006}$	$46.65^{+0.04}_{-0.02}$	26.2	Sluse et al. (2012)
J1042+1641	4	2.25	CO (10–9)	700 ± 120	140^{+140}_{-160}	9.31 ± 0.25	$0.65^{+0.02}_{-0.02}$	$48.34^{+0.02}_{-0.02}$	117	Glikman et al. (2018a), this work
SDSS J1330+1810	4	1.39	CO (7–6)	190 ± 20	150^{+160}_{-80}	-	$0.05^{+0.03}_{-0.02}$	$46.66^{+0.04}_{-0.04}$	68.2	Blackburne et al. (2011); Stacey et al. (2018), this work
			[CII] (2–1)	158 ± 5						This work
H1413+117	4	2.56	CO (9–8)	370 ± 10	1600 ± 60	9.12 ± 0.01	$0.06^{+0.06}_{-0.02}$	$47.93^{+0.04}_{-0.04}$	10.3	Stacey et al. (2021); Sluse et al. (2012)
			CO (3–2)	360 ± 20						Barvainis et al. (1997)
WFIJ2026–4536	4	2.23	CO (10–9)	252 ± 7	1010 ± 60	9.18 ± 0.36	$0.02^{+0.01}_{-0.01}$	$47.68^{+0.04}_{-0.02}$	33.0	Stacey et al. (2021); Comachione et al. (2020); Bate et al. (2018)
WFIJ2033–4723	4	1.66	CO (8–7)	80 ± 10	100 ± 30	8.63 ± 0.35	$0.03^{+0.05}_{-0.03}$	$47.08^{+0.06}_{-0.04}$	19.7	Stacey et al. (2021); Sluse et al. (2012); Morgan et al. (2004)
SDSS J0100+2802	1	6.33	CO (10–9)	380^{*}	2800 ± 1400	10.09 ± 0.07	$0.02^{+0.02}_{-0.01}$	$47.98^{+0.06}_{-0.04}$	-	Wu et al. (2015); Wang et al. (2019)
			[CII]	380 ± 20						Wang et al. (2019)
SDSS J1148+5251	1	6.42	CO (7–6)	300 ± 40	3600 ± 1200	9.43 ± 0.07	$0.02^{+0.02}_{-0.01}$	$47.30^{+0.04}_{-0.03}$	-	Carniani et al. (2019); Leipski et al. (2013); Gallerani et al. (2017)
			[CII]	287 ± 28						Walter et al. (2009)
BRII202–0725	1	4.70	CO (7–6)	316 ± 40	3200 ± 1600	9.1 ± 0.3	$0.020^{+0.005}_{-0.005}$	$47.66^{+0.01}_{-0.01}$	-	Salomé et al. (2012); Carniani et al. (2013)
			[CII]	275 ± 15						Carilli et al. (2013)
ULAS J1234+0907	1	2.50	CO (7–6)	900 ± 80	2500 ± 900	10.4	$1.77^{+0.07}_{-0.07}$	$48.16^{+0.05}_{-0.04}$	-	Banerji et al. (2017, 2018)
			CO (3–2)	870 ± 60						Banerji et al. (2021)
SDSS J2310+1814	1	6.00	CO (9–8)	380 ± 20	4300 ± 700	9.6	$0.004^{+0.007}_{-0.003}$	$47.37^{+0.04}_{-0.03}$	-	Carniani et al. (2019); Li et al. (2020); Feruglio et al. (2018)
			[CII]	390 ± 20						Li et al. (2020)
ULAS2315+0143	1	2.57	CO (7–6)	580 ± 70	3000 ± 600	10.1	$1.27^{+0.07}_{-0.08}$	$47.66^{+0.05}_{-0.05}$	-	Banerji et al. (2017, 2018)
			CO (3–2)	300 ± 60						Banerji et al. (2021)

This paper has been typeset from a $\text{\TeX}/\text{\LaTeX}$ file prepared by the author.